Signal Processing and Analysis

Physics Informed Neural Networks for Electrical Impedance Tomography

Danny Smyl[1]*, Tyler Tallman[2], Laura Homa[3], Chenoa Flournoy[3], Sarah Hamilton[4], John Wertz[5]

[1] Department of Civil and Environmental Engineering, Georgia Institute of Technology, Atlanta, GA, 30332, USA
[2] School of Aeronautics and Astronautics, Purdue University, West Lafayette, IN 47907-2045, USA
[3] University of Dayton Research Institute, Dayton, OH, 45469, USA
[4] Department of Mathematical and Statistical Sciences, Marquette University, Milwaukee, WI, 53233, USA
[5] Air Force Research Laboratory, Composite, Ceramic, Metallic, Materials Performance Division, Materials State Awareness Branch, WPAFB, OH, 45433, USA

Abstract—Electrical Impedance Tomography (EIT) is an imaging modality used to reconstruct the internal conductivity distribution of a domain based on boundary voltage measurements. In this paper, we present a novel EIT approach for integrated sensing of composite materials and structures utilizing Physics Informed Neural Networks (PINNs). Unlike traditional data-driven only models, PINNs incorporate underlying physical principles governing EIT directly into the learning process, enabling precise and rapid reconstructions. We demonstrate the effectiveness of PINNs with a variety of physical constraints for integrated sensing. The proposed approach has the potential to enhance material characterization and condition monitoring, offering a robust alternative to classical EIT approaches.

Index Terms—Neural Networks, Machine Learning, Electrical Impedance Tomography, EIT, ERT, Nondestructive Evaluation, Sensing, Physics Informed Neural Networks

I. INTRODUCTION

Physics-Informed Neural Networks (PINNs) represent a powerful class of deep learning algorithms which incorporate physical laws directly into the neural network training process. Unlike traditional data-driven models that rely solely on large datasets, PINNs leverage governing partial differential equations (PDEs), or other known physical constraints, to regularize the network's training [1], [2]. This allows PINNs to operate effectively even with limited or noisy data, making them particularly well-suited for solving problems where obtaining high-quality training data is difficult or expensive [3]. By embedding the laws of physics into the loss function (and backpropagating these losses), PINNs enforce compliance with these equations during optimization, leading to solutions that are accurate *and* physically consistent [4].

In the context of inverse problems, PINNs are especially advantageous, yet their experimental validation is absent in EIT literature (we refer to [5]–[7] for numerical investigations). Inverse problems involve determining unknown parameters of or inputs to a system based on observations (measurements). These problems are generally ill-posed, meaning that they may not have unique or stable solutions, making traditional numerical methods prone to instability [8]. PINNs handle such ill-posed problems by incorporating physical laws directly into a learning framework, helping to regularize the inverse problem and guide the network towards physically meaningful solutions — thus promoting solutions with desired (physical) properties. This coupling of data and physics may allow PINNs to outperform purely data-driven models, particularly when the data is sparse or noisy.

Moreover, the flexibility of PINNs in handling both forward and inverse problems makes them versatile tools. For inverse problems, PINNs can be trained to minimize a combined loss that measures discrepancies between predicted and observed data, while simultaneously enforcing satisfaction of the governing equations. This results in the discovery of unknown parameters (in the case of EIT, conductivity fields), boundary conditions, or even source terms that are consistent with both the observed data and the underlying physics. The integration of these physical principles into the machine learning framework not only enhances the interpretability of the results, but also improves the robustness and generalization capabilities of the model, making PINNs a state-of-the-art approach in computational physics and engineering. In the following, we will first provide an outline for the PINN methodology used for EIT imaging and integrated sensing of composite materials and structures, highlight key experimental details, provide concise results and, lastly, present conclusions and future research avenues. **The ultimate aim of this work is to determine if PINNs can (a) outperform a conventional data-driven only NN and (b) match the fidelity of classical EIT imaging.** This will be tested using experimental measurements obtained from damaged composite structures.

Corresponding author: D. Smyl (e-mail: danny.smyl@ce.gatech).
(see https://www.ce.gatech.edu/directory/person/danny-smyl).
Associate Editor:

II. METHODOLOGY: PINN APPROACH

A. Overview

There exist numerous possible learned approaches for solving inverse problems [9]. In the context of EIT for integrated sensing, the aim is to develop a function $\mathcal{A}$ which maps voltage information directly to conductivity for rapid interpretation (e.g. for condition monitoring of composite structures). Here, the learnable EIT problem seeks to train a PINN to generate the following approximation:

$$\mathcal{A}(\Delta V) \approx \sigma \tag{1}$$

where ΔV, selected for robustness to systematic errors [10], are difference electrode potentials (subtraction of voltages measured in a reference state from voltages measured after a change in state) and σ is a representation of the true conductivity field which is normalized to the range $[0, 1]$. This range was selected due to the experimental test cases considered herein, where the conductivity distributions are binary due to localized structural damage. In our

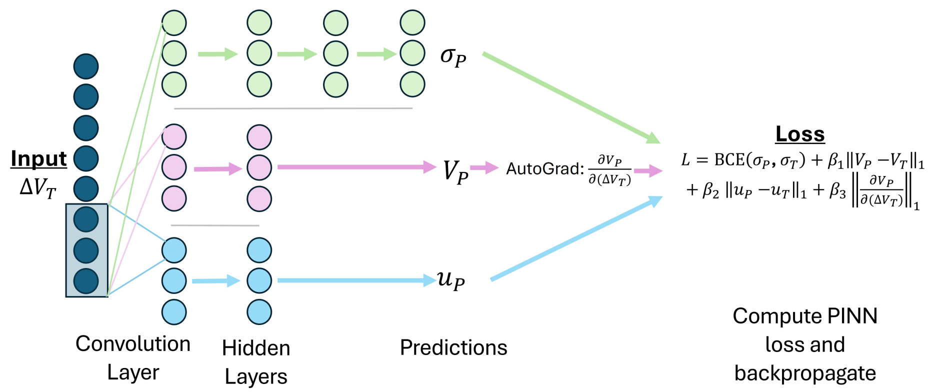

Fig. 1. Schematic illustration of the three tiered mixed classification/regression PINN architectures and approach used in this work.

approach outlined here, this is accomplished by minimizing a mixed classification-regression loss of the form:

$$L = \frac{1}{n}\sum_{i=1}^{n} \mathrm{BCE}(\sigma_p^i - \sigma_t^i) + L_{\mathrm{PINN}}^i \tag{2}$$

where

$$L_{\mathrm{PINN}}^i = \beta_1 \left\| V_p^i - V_t^i \right\|_1 + \beta_2 \left\| u_p^i - u_t^i \right\|_1 + \beta_3 \left\| \frac{\partial V_p^i}{\partial(\Delta V_t^i)} \right\|_1 \tag{3}$$

where subscripts 'p' and 't' refer to predicted and training, superscript i is a data index in a data set containing n samples, 'BCE' refers to the binary cross entropy loss, respectively, x and y are spatial coordinates, σ is the binary conductivity, V are electrode potentials, u are internal nodal potentials, w are network weights, and β_1, β_2, and β_3 are weighting coefficients treated as learnable parameters and initialized such that the loss terms were on the same order of magnitude. To ensure stability, the weighting coefficients (β_1, β_2, and β_3) were transformed using their logarithm to ensure positivity, projected via exponentiation during training, and regularized using an L_1 norm to avoid significant deviation from their initial values. No weight decay or weight regularization is applied.

B. PINN loss functions and network considerations

Through an initial exploration of the numerous possible physics loss functions, the following were found to provide suitable constraint for the imaging considered in this work.

Electrode potential loss function: Perhaps most straighforward of the physics losses, is the electrode potential loss function, which enforces the PINN to obey the forward model. The resulting loss term is as follows:

$$\text{Electrode potential PINN Loss} = \frac{\beta_1}{n}\sum_{i=1}^{n} \|V_p^i - V_t^i\|_1. \tag{4}$$

Internal potential loss function: The following internal potential loss term, also enforcing the PINN to obey the EIT forward model (internally) is given by:

$$\text{Spatial potential PINN Loss} = \frac{\beta_2}{n}\sum_{i=1}^{n} \|u_p^i - u_t^i\|_1. \tag{5}$$

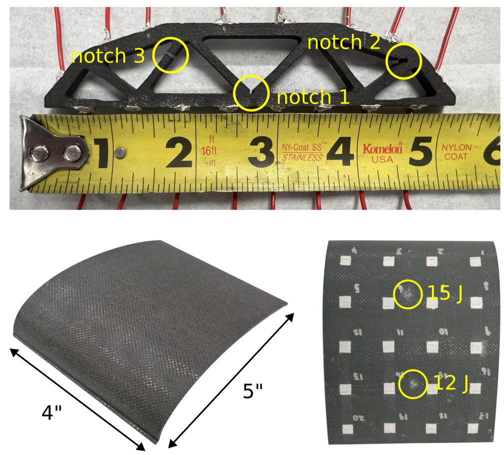

Fig. 2. Top: Carbon fiber truss specimen. Bottom: Carbon fiber/epoxy NACA 4424 specimen.

This function accounts for possible internal spikes in the potential field forcing the PINN to be physically realistic within the domain imaged.

Compatibility loss function: The final PINN term used ensures compatibility between network inputs and outputs. This constraint results from the static nature of the voltage terms, namely that the voltage after a change in state is fixed with respect to the voltage differences, resulting in the following loss:

$$\text{Compatibility PINN Loss} = \frac{\beta_3}{n}\sum_{i=1}^{n} \left\| \frac{\partial V_p^i}{\partial(\Delta V_t^i)} \right\|_1. \tag{6}$$

This results from the realization that V_p^i cannot change with respect to a fixed input ΔV_t^i, thus we aim to enforce $\frac{\beta_3}{n}\sum_{i=1}^{n} \left\| \frac{\partial V_p^i}{\partial(\Delta V_t^i)} \right\| \to 0$.

General network parameters and training. All regression loss norms are L_1 to avoid outlier spiking. Batch sizes of 16, initial learning rate at 10^{-5} with exponential decay, $\gamma = 0.99$, dropout rate of 50%, LeakyReLU activation and a convolutional input feature layers were selected. To avoid cross talk between conductivity and physics parameters, the input layers were split into three adjacent networks—using a deeper network with skip connections for conductivity predictions to improve fidelity—shown schematically in Figure 1.

To train the networks in both experimental cases considered in the forthcoming sections, a total of 50,000 training samples per case were generated using randomized low conductivity fields (blobby

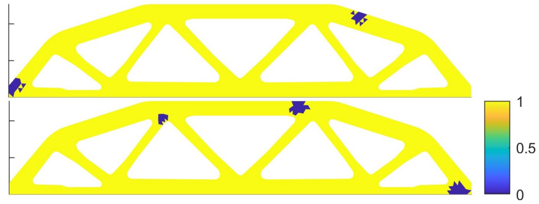

Fig. 3. Random binary conductivity training data samples.

inclusions within a homogeneous background computed using the best homogeneous estimate — see Figure 3 for representative images) with 0.1% standard deviation Gaussian noise added to input data for regularization. From these data sets, 10,000 samples were removed for validation. Within each epoch, 10,240 samples were randomly subsampled from the entire dataset to improve generalization and better handle data throughput. Training was then conducted using PyTorch [11] on Nvidia GPUs (RTX 4090/A2000) for 300 epochs per trial (to prevent overfitting). In order to compute derivatives in PINN loss terms, the AutoGrad function was utilized.

III. EXPERIMENTAL STUDIES

A. Damaged carbon fiber truss

The first experimental study was performed on an additively manufactured carbon fiber truss structure produced by Impossible Objects. The manufacturing process is described in reference [12]. Three instances of notch damage were induced by a hacksaw, and notch locations were selected based on likely damage formation during four-point bending as determined by discrete damage modeling [13]. A total of 16 electrodes were placed roughly equidistantly along the outer edge of the truss. Electrodes were made by using a combination of silver paint (Ted Pella 16040-30) and silver epoxy (mg Chemicals 8331D) to adhere wires to the truss. A Mastech HY3005D-3 power supply was then used to inject 0.5 DC, while a National Instruments with one PXI-8386 and two PXI-6123 cards were used to measure voltages. An adjacent-adjacent injection-measurement pattern was used. The experimental setup is shown to the left in Figure 2. For additional experimental details, interested readers are directed to reference [14].

B. Damaged carbon fiber airfoil

The second experimental study was performed on a plain weave carbon fiber (Fibre Glast)/epoxy (Fibre Glast System 2000 Laminating Epoxy Resin) composite laminate shaped as a representative NACA 4424 airfoil with a width of 4” and a chord length of 5”. The laminate used a total of 15 layers of carbon fiber. Stacking was done in a female mold machined out of aluminum and using the wet layup plus vacuum bagging technique. After curing the airfoil and trimming it to its final shape, it was twice impacted (at different locations) in a CEAST 9340 drop tower. The first impact was at 15 J, and the second impact was at 12 J. Impact locations are shown in the right of Figure 2. A total of 20 electrodes were attached to the top surface using silver paint (Ted Pella 16040-30). Direct Current of 0.8 A was injected using a BK Precision 9131 B power supply while voltages were measured using a National Instruments PXIe-6368 data acquisition system. Current injections and voltage measurements were done in a ‘snake-like’ pattern. For more details on the injection-measurement pattern and experimental details in general, interested readers are directed to reference [15].

IV. RESULTS AND DISCUSSION

A. EIT imaging results

To answer the research questions highlighted in Section I, we compare PINN reconstructions to data-driven only neural network and nonlinear difference imaging reconstructions (NLDI—classical imaging, following [16] with a smoothness prior used for background conductivity and Laplace regularized change in conductivity, $\Delta\sigma$). To ensure fair comparison, the data-driven only network utilizes the same architecture used in the PINN conductivity classifier along with the same BCE loss function.

We first analyze the damaged truss case where reconstructions using all three EIT approaches are reported in Figure 4. In this experiment, we observe that all three EIT reconstruction frameworks capture damage for both cases considered. However, PINN reconstructions most clearly localize the notches and provide the fewest background artifacts. In contrast, both the classical and data-driven approaches contain obvious fluctuations in background conductivity. While comparing the PINN and data-driven reconstructions, we note that the PINN images provide significantly lower conductivity values at the location of the notches (which should be near zero as these areas are void of conductive material).

In the higher dimensional (output) experimental case, we examine the 3D airfoil reconstructions, containing approximately 10 times more inverse degrees of freedom than the truss experiment. These imaging results are reported in Figure 5 where, again, all three frameworks capture the dual damages well. Upon initial observation, we notice that the PINN reconstruction provides a tighter localization of the 15 J impact and a clearer representation of the 12 J impact than the data-driven only approach. In comparison, the classical reconstruction captures the 15 J impact damage comparably to the data-driven approach, with some sparse observed background artifacts. Further discussion of these results follows below.

B. Discussion

The aim of the paper was to determine if PINNs are capable of (a) outperforming a conventional data-driven only NN and (b) matching the fidelity of classical EIT imaging approaches. The answer to these queries is qualitatively **yes**, which was demonstrated in the experimental investigation provided in the Section IV-A. While the fidelity of classical inversion approaches vary considerably and are subject to parameterization, regularization, discretization, and numerous other factors outside the scope of this work, what remains to question is: why did PINNs outperform the data-driven NNs?

Some insight into this query can be obtained from the loss plot shown in Figure 6, where we see an overlay of the PINN losses with the total losses. We observe that, in our PINN formulation, the physics terms (orange line in 6) provide significant constraint on the learning process, especially in the initial portion of training. This implies that the network is forced to adhere to problem physics before significantly minimizing the data loss. Such regularization clearly improves the validation curve, which is shown to converge smoothly after initial training. Based on these realizations, we infer

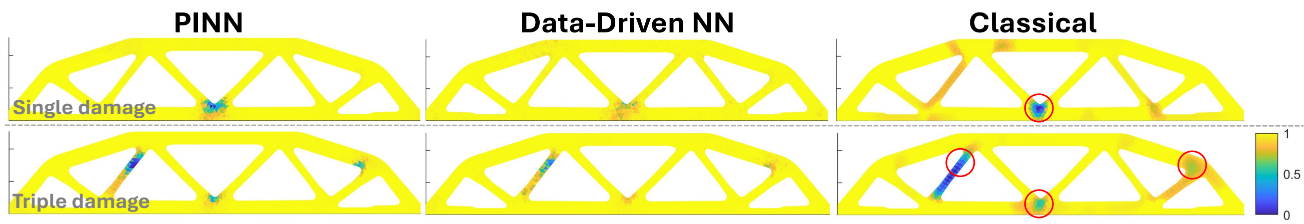

Fig. 4. Reconstructions of a damaged truss: top row, one notch and bottom row, three notches. Dimensions are in meters and reconstructions are reported in a scale of [1,0]. Damage locations are circled in red atop the classical reconstructions.

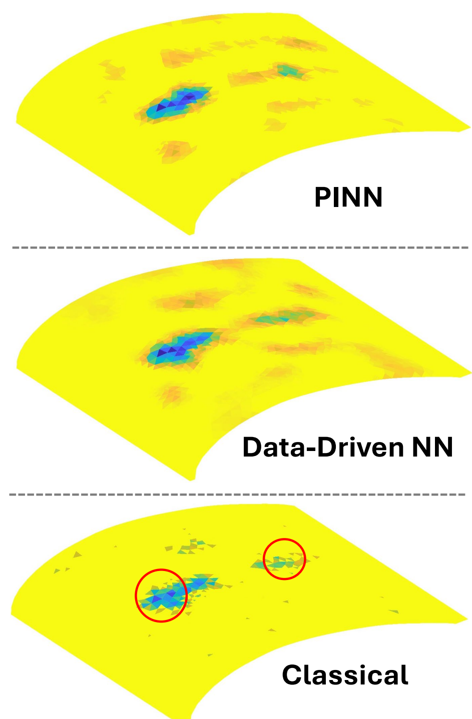

Fig. 5. Reconstructions of a damaged airfoil with dual impacts. Dimensions are in meters and images are reported in a [1,0] scale with the same coloring as Figure 4. Damage locations are circled in red.

that the improvements brought on by physics-based regularization in PINNs provide superior generalization in the context of the sparse binary nature of the conductivity training samples (cf. Figure 3). Ultimately, the enhanced generalization of PINNs resulted in improved localization and more realistic conductivity estimation at damage locations than the data-driven only models.

In addition to the former points, PINN frameworks provide avenues for adapting to training dynamics that the present data-driven approach does not possess. For example, one could argue that the ability to automate loss coefficients improves the ability of the network to avert local minimums, compatibility constraints enforce physically-realistic connections between inputs and outputs and the inclusion of internal information (i.e. u) provides information relating spatial physical dependencies to inverse causalities of interest (in this work σ). In eventuality, however, additional terms, such as spatial gradients of u, higher order derivatives and other compatibility terms need to be investigated to fully understand the the influence of physics constraints on the fidelity of EIT reconstructions using PINNs.

Lastly, from a numerical standpoint, it is worth remarking that the PINN approach adopted herein is substantially more computationally demanding than the data-driven NN approach. Indeed, the PINNs required approximately a factor of five more parameters to estimate than the data-driven NNs, resulting in nearly the same factor more training time (on the RTX-4090 machine). This computing hurdle can be alleviated in future works where regression only predictions are made, whereby automatic mixed precision is available when BCE loss is not utilized. Ultimately, however, the trade-off in training time for the PINNs is leveraged by ≈80,000x speedup in solving the EIT problem relative to the classical approach.

V. CONCLUSIONS

This work affirmed the feasibility of PINNs for EIT imaging through an experimental investigation exploring the reconstruction of damage in composite structures. It was found that PINNs are capable of (a) outperforming a conventional data-driven NN and (b) matching the fidelity of classical EIT inversion approaches. Discussion was provided on key features that promoted improved generalization of PINNs relative to data-only EIT imaging and provided future avenues for PINN research applied to EIT imaging.

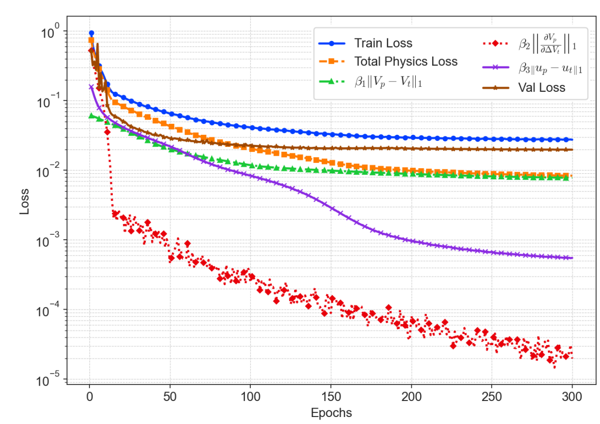

Fig. 6. PINN training losses demarcating individual physics terms.

VI. AUTHOR CONTRIBUTION STATEMENT

Danny Smyl conceived of this work, developed the PINN constraints, and provided most of the writing; Tyler Tallman provided data for testing, EIT subject matter expertise, and edited the writing; Laura Homa provided data for training, input on the PINN constraints, and edited the writing; Chenoa Flournoy provided input on development of the PINN and PINN constraints; Sarah Hamilton supported the background literature review and edited the writing; and John Wertz helped conceive of the work, provided data for testing, and edited the writing.

REFERENCES

[1] Zheyuan Hu, Khemraj Shukla, George Em Karniadakis, and Kenji Kawaguchi. Tackling the curse of dimensionality with physics-informed neural networks. *Neural Networks*, 176:106369, 2024.

[2] Majid Rasht-Behesht, Christian Huber, Khemraj Shukla, and George Em Karniadakis. Physics-informed neural networks (pinns) for wave propagation and full waveform inversions. *Journal of Geophysical Research: Solid Earth*, 127(5):e2021JB023120, 2022.

[3] Jassem Abbasi and Pål Østebø Andersen. Physical activation functions (pafs): an approach for more efficient induction of physics into physics-informed neural networks (PINNs). *Neurocomputing*, 608:128352, 2024.

[4] George Em Karniadakis, Ioannis G Kevrekidis, Lu Lu, Paris Perdikaris, Sifan Wang, and Liu Yang. Physics-informed machine learning. *Nature Reviews Physics*, 3(6):422–440, 2021.

[5] Xuanxuan Yang, Yangming Zhang, Haofeng Chen, Gang Ma, and Xiaojie Wang. A two-stage imaging framework combining cnn and physics-informed neural networks for full-inverse tomography: A case study in electrical impedance tomography (eit). *arXiv preprint arXiv:2407.17721*, 2024.

[6] Akarsh Pokkunuru, Pedram Rooshenas, Thilo Strauss, Anuj Abhishek, and Taufiquar Khan. Improved training of physics-informed neural networks using energy-based priors: a study on electrical impedance tomography. In *The Eleventh International Conference on Learning Representations*, 2023.

[7] Leah Bar and Nir Sochen. Strong solutions for pde-based tomography by unsupervised learning. *SIAM Journal on Imaging Sciences*, 14(1):128–155, 2021.

[8] A. Gallet, S. Rigby, T. N. Tallman, X. Kong, I. Hajirasouliha, A. Liew, D. Liu, L. Chen, A. Hauptmann, and D. Smyl. Structural engineering from an inverse problems perspective. *Proceedings of the Royal Society A: Mathematical, Physical and Engineering Sciences*, 478(2257):20210526, January 2022.

[9] Andreas Hauptmann, Jonas Adler, Simon Arridge, and Ozan Öktem. Multi-scale learned iterative reconstruction. *IEEE transactions on computational imaging*, 6:843–856, 2020.

[10] Valentina Candiani, Nuutti Hyvönen, Jari P Kaipio, and Ville Kolehmainen. Approximation error method for imaging the human head by electrical impedance tomography. *Inverse Problems*, 37(12):125008, 2021.

[11] Adam Paszke, Sam Gross, Francisco Massa, Adam Lerer, James Bradbury, Gregory Chanan, Trevor Killeen, Zeming Lin, Natalia Gimelshein, Luca Antiga, et al. Pytorch: An imperative style, high-performance deep learning library. *Advances in neural information processing systems*, 32, 2019.

[12] Dongjin Kim, Jaewook Lee, Tsuyoshi Nomura, Ercan M Dede, Jeonghoon Yoo, and Seungjae Min. Topology optimization of functionally graded anisotropic composite structures using homogenization design method. *Computer Methods in Applied Mechanics and Engineering*, 369:113220, 2020.

[13] Endel V Iarve, Kevin H Hoos, Yuriy Nikishkov, and Andrew Makeev. Discrete damage modeling of static bearing failure in laminated composites. *Composites Part A: Applied Science and Manufacturing*, 108:30–40, 2018.

[14] Tyler N Tallman, Laura Homa, Mark Flores, and John Wertz. Damage mapping via electrical impedance tomography in complex am shapes using mixed smoothness and bayesian regularization. *Computer Methods in Applied Mechanics and Engineering*, 414:116185, 2023.

[15] Monica Sannamani, Jinling Gao, Weinong W Chen, and Tyler N Tallman. Damage detection in non-planar carbon fiber-reinforced polymer laminates via electrical impedance tomography with surface-mounted electrodes and directional sensitivity matrices. *Composites Science and Technology*, 224:109429, 2022.

[16] Danny Smyl, Mohammad Pour-Ghaz, and Aku Seppänen. Detection and reconstruction of complex structural cracking patterns with electrical imaging. *NDT & E International*, 99:123–133, 2018.